Thermally Induced Anomaly in the Shear Behavior of Magnetite at High Pressure

Yongtao Zou, Wei Zhang, Ting Chen, Xing-ao Li, Chun-Hai Wang, Xintong Qi, Shanmin Wang, Tony Yu, Bingbing Liu, Yanbin Wang, Robert C. Liebermann, Yusheng Zhao, and Baosheng Li

Novel thermal-induced anomaly in the shear behavior of Fe_3O_4 magnetite at high pressure

Yongtao Zou,[1,2,*] Wei Zhang,[3] Ting Chen,[2] Xing-ao Li,[4] Chun-Hai Wang,[1] Xintong Qi,[2] Shanmin Wang,[1] Tony Yu,[5] Bingbing Liu,[6] Yanbin Wang,[5] Robert C. Liebermann[2], Yusheng Zhao,[1,*] and Baosheng Li[2,*]

[1]*Academy for Advanced Interdisciplinary Studies, and Department of Physics, Southern University of Science and Technology, Shenzhen, 518055, China*

[2]*Mineral Physics Institute, and Department of Geosciences, State University of New York, Stony Brook, N.Y. 11794, United States*

[3]*School of Science, Southwest University of Science and Technology, Mianyang, Sichuan 610064, China*

[4]*School of Science, Nanjing University of Posts and Telecommunications, Nanjing 210046, China*

[5]*Center for Advanced Radiation Sources, The University of Chicago, Chicago, I.L. 60637, United States*

[6]*State Key Laboratory of Superhard Materials, Jilin University, Changchun, 130012, China*

E-mail: zouyt@sustc.edu.cn; zhaoys@sustc.edu.cn; baosheng.li@stonybrook.edu;

ABSTRACT

Thermoelasticity and acoustic/phonon velocities of polycrystalline magnetite have been studied at simultaneously high pressures and temperatures up to 8.6 GPa and 1123 K using ultrasonic interferometry in conjunction with *in situ* x-ray techniques. Here, we have discovered temperature-driven anomalies in the shear behavior at temperatures up to ~450 K, together with pressure-induced softening in the shear properties. Fitting the current data to finite strain equations, we obtain the bulk and shear moduli, as well as their pressure and temperature dependences, namely B_{S0} =173.2(5) GPa, G_0 = 55.5(2) GPa, $\partial B_S/\partial P$ = 2.99(9), $\partial G/\partial P$ = -0.23(3),

25 $\partial B_S/\partial T$ = -0.0209(10) GPa/K, $\partial G/\partial T$ = 0.0042(4) GPa/K, $(\partial^2 Bs/\partial T^2)_P$ = -1.7(1)×10⁻⁵ GPa²/K² and

26 $(\partial^2 G/\partial T^2)_P$ = -2.5(1)×10⁻⁵ GPa²/K². The origin of the thermal-induced anomaly in the shear

27 modulus for Fe_3O_4 magnetite is ascribed to the coupling of local atomic distortions and

28 short-range charge ordering of six-coordinated Fe^{2+}-Fe^{3+} ions at the octahedral sites in the

29 inverse-spinel structure. These findings/results provide us new high-P thermoelasticity data of

30 magnetite, and open a window for good understanding of the underlying mechanism for

31 temperature-driven anomaly in magnetite-based solid solutions and spinel-structured materials

32 for their applications in extreme conditions.

33

36

37 **I. INTRODUCTION**

38 Magnetite (Fe_3O_4) has attracted great interest because of the importance of understanding

39 the properties of spinel-structured materials and iron oxides in the Earth's interior, as well as its

40 industrial applications in magnetic/electronic materials and nanocomposites for its physical

41 behaviors [1-12]. At ambient conditions, magnetite is half-metallic and has an inverse spinel

42 structure, in which the tetrahedral four-coordinated A site is occupied by Fe^{3+}, and the octahedral

43 B site is occupied by both Fe^{2+} and Fe^{3+}. Because the magnetic moments of Fe ions are

44 anti-parallel at the tetrahedral and octahedral sites, magnetite exhibits a ferromagnetic state

45 below the Curie temperature of ~860 K [13]. At ambient pressure, magnetite underwent

46 metal-insulator transition below the Verwey temperature ($T_V \approx$ 122 K) where an abrupt increase

47 of electrical resistivity was observed in association with a cubic-to-monoclinic phase transition

48 [14]. Above the Verwey transition, it is accepted that the inverse-spinel structured magnetite

49 adopts with Fe^{3+} ions in A sites and B sites in a mixed valence $Fe^{2.5+}$ state [15-20]. However,

50 several previous studies indicated the existence of short-range order of polaronic character

51 [15-20], which is correlated with the critical softening of C_{44} elastic constant on cooling [15,16],

52 softening of the surface phonons [17], low-energy fluctuations of the lattice distortions [18],

53 anomalous phonon broadening [19] and the Fermi surface nesting features [20]. However, to date,

54 the short-range ordering and/or its related abnormal properties above the Verwey transition or at

55 temperatures higher than ~122 K is still not well understood.

56   Recently, high-pressure studies on magnetite have raised enormous controversies about the

57 interpretation of the electronic and structural behavior at pressures between 6 and 16 GPa [8, 9,

58 14, 21-25], ranging from the inverse-normal spinel transition [14], iron high-spin to

59 intermediate-spin transition [3, 21], pressure-tuned ideal inverse-spinel structure [23], and the

60 decreased Fe-O bond length caused by the discontinuous changes in the local oxygen coordinates

61 [24]. Recently, *in situ* magnetoresistivity measurements revealed a magnetoresistivity transition

62 at pressure of ~6.0 GPa owing to the half-metal to metal transition [8], in agreement with the

63 previous electrical resistivity measurement on the metallization of magnetite at room temperature

64 and pressures above 8 GPa [9]. However, the more recent studies on magnetite at high pressure

65 by Lin *et al* [25] using the combination of inelastic x-ray scattering, x-ray diffraction and Raman

66 spectroscopy techniques proposed that the origin of the abnormal elastic and vibrational

67 behaviors of magnetite at ~8 GPa was due to the local site distortions and the charge-ordering

68 between Fe^{2+} and Fe^{3+} ions at the octahedral sites in the inverse spinel.

69   Elastic bulk and shear moduli as well as their pressure and temperature dependences are

70 important parameters in understanding the high *P-T* behavior and physical properties upon

compression. The compressibility and bulk modulus (B) of magnetite have been studied by static compression experiments [21, 23, 25-31] and first-principles calculations [8, 32], however, the reported values are quite scattered with significant discrepancies, ranging from 155 to 215 GPa with the associated pressure derivative (B') in a wide range of 2.9 to 7.5. Sound velocities of single-crystal magnetite at high pressure were studied by Isida *et al* [33] up to 1.2 kbar, and the pressure dependences of the elastic constants C_{11} and C_{44} were reported to be anomalous. Recently, elasticity of a natural magnetite was measured at pressures up to 8.7 GPa using gigahertz ultrasonic interferometry in a diamond-anvil-cell [34], yielding a pressure-marker dependent $\partial B_S/\partial P$, namely $\partial B_S/\partial P = 5.1(1)$ for quartz pressure marker and $\partial B_S/\partial P \approx 3$ for ruby pressure scale, together with a negative $\partial G/\partial P = -0.1(1)$.

To date, the high-pressure behavior of magnetite is still in debate and studies under high temperature are rather scarce, especially for the shear-related properties. In this study, for the first time, simultaneous high-pressure and high-temperature sound velocity measurements on polycrystalline Fe_3O_4 magnetite have been conducted in a multi-anvil apparatus using ultrasonic interferometry in conjunction with x-ray diffraction/radiographic imaging techniques [34-39]. Here, we report the observations of temperature-driven and pressure-induced anomalies in the shear modulus of Fe_3O_4 magnetite, as well as the possible mechanisms underlying these abnormal behaviors. An internally consistent set of thermoelasticity for magnetite was derived based on the measured velocities and density data using a pressure-standard-free fitting procedure using the third-order finite strain equations [37].

II. EXPERIMENTAL DETAILS

The polycrystalline Fe_3O_4 magnetite specimen used in the present study was commercially

94   obtained from Trans-Tech. Inc., USA. Compressional (P) and shear (S) wave velocities of

95   polycrystalline Fe_3O_4 magnetite at high pressure and high temperature were measured using

96   ultrasonic interferometry in conjunction with *in situ* x-ray diffraction/x-radiography in a

97   multi-anvil apparatus at GSECARS (Sector 13) of Advanced Photon Source (APS), Argonne

98   National Laboratory. Details of this experimental setup were described elsewhere [35-39].

99   Briefly, the pressure-transmitting medium was MgO octahedron. Graphite was used as a heater.

100   A dual-mode $LiNbO_3$ transducer (10° Y-cut) was mounted with a high-temperature epoxy on a

101   truncated corner of a WC anvil cube, which can generate and receive both P and S signals

102   simultaneously. To minimize the loss of acoustic energy, all surfaces along the acoustic path,

103   including the ends of the WC cube with transducer mounted, alumina buffer rod and the

104   specimen, were well polished using 1 μm diamond paste. Inside the cell assembly, the front

105   surface of the sample was in contact with an alumina (Al_2O_3) buffer rod via a gold film (2 μm) to

106   improve their mechanical coupling, whereas the rear surface of the sample was backed by a

107   pressure marker NaCl. Temperatures were monitored with a $W_{97}Re_3$-$W_{75}Re_{25}$ thermocouple.

108   Travel times for P and S waves were simultaneously measured using the transfer function

109   method with standard deviation of ~0.4 ns for S waves and ~0.2 ns for P waves [35-39]. The

110   sample length at high pressure and high temperature was directly obtained by x-radiographic

111   imaging method; the precision of this direct measurement of sample length was estimated to be

112   0.2-0.4% [37, 38]. During our experiments, x-ray diffraction patterns for both the specimen and

113   pressure marker are collected using a solid-state detector, which is mounted on a stage behind the

114   high-pressure press set at a diffraction angle of $2\theta \approx 6.09°$. The collected x-ray diffraction

115   patterns of the sample are refined to determine the unit-cell volume, from which the densities at

116   high pressures and temperatures are obtained, as shown in TABLE SI.

III. RESULTS AND DISCUSSION

At ambient conditions, the polycrystalline Fe_3O_4 magnetite specimen has an inverse-spinel structure (space group: $Fd\bar{3}m$, No. 227), and the crystal structure is shown in Fig. 1(a). Prior to our ultrasonic measurement experiments, the purchased polycrystalline magnetite specimen was characterized by x-ray diffraction and SEM observations, showing that the starting magnetite was a pure cubic spinel structure and free of visible microcracks. SEM images of the recovered specimen from the current ultrasonic measurements show that the specimen exhibited an equilibrated and homogeneous microstructure without significant grain growth after annealing at the highest P-T conditions of 8.6 GPa and 1123 K, as shown in Fig. 1(b). After annealing and resintering at ~8.6 GPa and 1123 K, the bulk density of the recovered magnetite specimen from this study by Archimedes immersion method is ~5.18(2) g/cm^3, reaching ~99.5 % of the theoretical density of 5.21 g/cm^3. This means that the porosity of the specimen is about 0.5%, resulting in a negligible effect on the elasticity of polycrystalline magnetite within uncertainties [35-39]. SEM-EDX measurements on the recovered specimen yield a slightly nonstoichiometric composition of $Fe_{2.98(1)}O_4$, which is exactly the same value with the starting counterpart within uncertainties. A typical x-ray diffraction pattern of magnetite at the peak P-T conditions of 8.6 GPa and 1123 K is shown in Fig. 1(c), indicating that the specimen is still a spinel-structured material, and no other phases such as wüstite or hematite are observed.

The schematic experimental setup and P-T path for the present ultrasonic measurements in conjunction with synchrotron x-ray study are shown in Fig. S1(a) and S1(b), respectively. In this experiment, we performed four heating/cooling cycles at pressures up to ~8.6 GPa and temperatures up to 1123 K. The sample was annealed at a peak temperature of each cycle for several minutes to release nonhydrostatic stress accumulated during cold

140 compression/decompression. All the ultrasonic and x-ray diffraction measurements were

141 conducted along cooling after annealing at high pressures. Representative acoustic signals

142 observed at the peak P-T conditions of ~8.6 GPa and 1123 K are shown in Fig. 1(d). It is found

143 that echoes from the interfaces of anvil-buffer rod, buffer rod-sample, and sample-pressure

144 marker can be clearly identified, ensuring a precise determination of the compressional and shear

145 travel times even at the highest P-T conditions.

146 Comparison of x-ray diffraction patterns of magnetite at various pressures and temperatures

147 is shown in Fig. 2(a), indicating that no structural phase transitions/transformations occurred in

148 magnetite during the current measurements up to ~8.6 GPa and 1123 K. On the basis of the

149 travel time and sample length data in Table SI, the compressional (V_P) and shear (V_S) velocities

150 of Fe_3O_4 magnetite are derived. As shown in Fig. 2(b), while V_P increases monotonically with

151 pressures, however, V_S exhibits an anomalous negative pressure dependence. By fitting the

152 present acoustic velocity data to the third-order finite strain equations [35-38], we obtain $V_P =$

153 6.90(2) km/s and V_S = 3.28(2) km/s at ambient conditions. Our current data are ~4% lower than

154 those derived from single-crystal measurements on natural magnetite (V_P = 7.16(3) km/s; V_S =

155 3.41(2) km/s) by Reichmann et al [34]. As clearly seen in Fig. 2(b), our negative

156 pressure-dependence of shear velocity ($\partial V_S/\partial P \approx$ -0.017(3) km/s·GPa^{-1}) is almost the same as the

157 negative values for the natural magnetite [34] and for $NiFe_2O_4$ spinel [40]. By contrast, the

158 pressure dependence of V_P from this study, $\partial V_P/\partial P \approx$ 0.019(2) km/s·GPa^{-1}, is significantly

159 smaller than $\partial V_P/\partial P \approx$ 0.047(1) km/s·GPa^{-1} for the natural magnetite [34] and $\partial V_P/\partial P \approx$ 0.044(1)

160 km/s·GPa^{-1} for $NiFe_2O_4$ spinel [40], respectively.

161 As shown in Fig. 2(c), our obtained bulk moduli are consistent with those from the recent

162 inelastic x-ray scattering measurements on a stoichiometric single-crystal Fe_3O_4 magnetite by

163 Lin *et al* [25] within ~6.2 GPa, but lower than those from the gigahertz ultrasonic interferometry

164 in a diamond-anvil-cell on natural magnetite by Reichmann *et al* [34]. By contrast, however, our

165 derived shear moduli are in general agreement with those from previous studies using different

166 specimens and techniques [7,34], and no visible discontinuity is observed at pressures up to ~7.4

167 GPa in Fig. 2(c). To closer examine the structural stability of magnetite upon compression,

168 electrical resistance measurements have been conducted at pressures up to ~12.8 GPa in a

169 multi-anvil apparatus [see Fig. S2(a)]. It is found that the resistance decreases continuously with

170 increasing pressures, indicating that the magnetite specimen becomes a better metallic conductor

171 at higher pressures. This result agrees well with the previous studies on the electrical resistivity

172 of magnetite at high pressure [9, 21, 25].

173   Fig. 3(a) shows the compressional and shear wave velocities of Fe_3O_4 magnetite along

174 different isotherms under high pressure. The compressional wave velocity exhibits a systematic

175 increase with pressures and decreases with temperatures, whereas the shear wave velocity (V_S)

176 shows a negative trend as a function of pressure along all the isothermal temperatures ranging

177 from 300 to 1123 K. The current negative pressure dependence in V_S ($\partial V_S/\partial P$ = -0.017(3) km

178 s^{-1}/GPa) is in great contrast to previous reports for other spinel-structured materials, such as

179 $MgAl_2O_4$ ($\partial V_S/\partial P$ = 0.0022(5) km s^{-1}/GPa) [Ref. 38] and Mg_2SiO_4 ($\partial V_S/\partial P$ = 0.021 km s^{-1}/GPa)

180 [Ref. 41]. As suggested for natural magnetite, the negative pressure dependence is originated

181 from the softening shear constant C_{44} under pressures [34]. A closer examination of Fig. 3(a)

182 indicates that, in addition to the negative pressure dependence in V_S, the shear wave velocities

183 appear to exhibit a positive temperature dependence within 300 and 673 K (see Fig. 3a) and then

184 change to a negative dependence above 673 K. This abnormal behavior as a function of

185 temperature has never been observed in magnetite before.

186   The bulk and shear moduli are calculated using $\rho V_P^2 = B_S + 4G/3$ and $G = \rho V_S^2$, respectively,

187   based on acoustic/phonon velocities and densities (Table SI), and the results are shown in Fig.

188   3(b). Clearly, the thermal-induced anomaly in V_S is also observed in the derived shear moduli.

189   We fit all the data collected in the entire P-T conditions of this study to the third-order

190   finite-strain equations to obtain adiabatic ambient-condition bulk and shear moduli as well as

191   their pressure and temperature derivatives/dfependences. The detailed data-processing procedure

192   can be found elsewhere [35-38]. With the thermal expansivity $\alpha = 1.425 \times 10^{-5} + 3.65 \times 10^{-8} T$ (Ref.

193   42) and Grüneisen parameter $\gamma = 1.33$ from Ref. 33, we obtained the elastic bulk and shear

194   moduli, as well as their pressure and temperature dependences, namely B_{S0} =173.2(5) GPa, G_0 =

195   55.5(2) GPa, $\partial B_S/\partial P$ = 2.99(9), $\partial G/\partial P$ = -0.23(3), $\partial B_S/\partial T$ = -0.0209(10) GPa/K, $\partial G/\partial T$ =

196   0.0042(4) GPa/K, $(\partial^2 B_S/\partial T^2)_P$ = -1.7(1)×10^{-5} GPa^2/K^2 and $(\partial^2 G/\partial T^2)_P$ = -2.5(1)×10^{-5} GPa^2/K^2 (see

197   Table I). We note, for most minerals/materials, the cross derivatives of $(\partial^2 B_S/\partial P \partial T)_P$ and

198    $(\partial^2 G/\partial P \partial T)_P$ are on the order of 10^{-4} (Refs. 37, 38), resulting in an overall effect on the pressure

199   derivatives with an order of ~0.1, which is negligible and thus assumed to be zero in this study.

200   The elasticity of Fe$_3$O$_4$ magnetite is summarized in Table I for comparison with those from

201   previous studies on magnetite, wüstite, and other spinel-structured materials

202   [8,26,31,34,38,40-44]. The bulk modulus (B_{S0}=173.2(5) GPa) of Fe$_3$O$_4$ magnetite from this

203   study is generally consistent with the previous experimental data [183(10) and 215(25) GPa from

204   Refs. 26 and 31] and theoretical results of 182(9) GPa [8] within the mutual uncertainties, but is

205   ~7% lower than that for natural magnetite [34] as well as that by theoretical calculations [43]. As

206   shown in Table I, the pressure derivative of $\partial B_S/\partial P$ =2.99(9) from this study is in excellent

207   agreement with the recent theoretical result (B' = 2.90(1)) [8]. On the other hand, our obtained

208   shear modulus of G_0=55.5(2) GPa is significantly lower than that for natural magnetite [34] , but

209 larger than the theoretical result of 49.5 GPa [43]. These discrepancies may result from the

210 different pressure ranges and hydrostatic conditions in different experimental studies as well as

211 the well-known trade-off between the bulk modulus and its pressure derivative in

212 equation-of-state fit.

213 As clearly seen in Table I, the unusual negative pressure dependence of shear modulus

214 ($\partial G/\partial P$ = -0.23(3)) for Fe_3O_4 magnetite from this study is generally consistent with $\partial G/\partial P$ =

215 -0.1(1) for natural magnetite [34] within the mutual uncertainties, but is significantly lower than

216 the weak positive-values for non-silicate spinels (*e.g.* $\partial G/\partial P$ = 0.58 for $MgAl_2O_4$ spinel [38] and

217 $\partial G/\partial P$ = 0.38 for $NiFe_2O_4$ trevovite [40]), as well as the large positive $\partial G/\partial P$ =1.5 for Mg_2SiO_4

218 silicate spinel [45]. Likely, the origins for the pressure-induced abnormal shear behavior in

219 spinel-structured Fe_3O_4 magnetite (G' = -0.23) include both the FeO_6 octahedral distortion upon

220 compression as proposed by Zou *et al* [38] for non-silicate spinels, and the magnetoelastic

221 coupling as well as the first-order phase transition to an orthorhombic structure at high pressure

222 by Reichmann *et al* [34].

223 To gain insight into the mechanism for the thermal-induced anomaly in the shear properties,

224 the shear modulus for Fe_3O_4 magnetite as a function of temperature at constant pressure is

225 calculated based on our newly derived thermoelasticity data (Fig. 4a), which are compared with

226 those for iron-bearing compounds such as $Fe_{0.943}O$ wüstite and Fe_2TiO_4 ulvöspinel, as well as

227 other spinel-structured materials (see Figs. 4b and 4c). As shown in Fig. 4(a), the shear modulus

228 for Fe_3O_4 magnetite increases with temperatures and reaches a maximum value of ~55.8 GPa at

229 the temperature of ~450 K, above which it decreases with increasing temperature. As shown in

230 Fig. 4(c), this anomalous behavior is quite similar to those of $Fe_{0.943}O$ wüstite and Fe_2TiO_4

231 ulvöspinel, but is significantly different from the trends for Al- and Fe-bearing spinels such as

232   NiFe$_2$O$_4$, MgFe$_2$O$_4$ and MgAl$_2$O$_4$, where the shear moduli decrease gradually with temperatures.

233   To seek a possible structure-related mechanism for the thermal-induced anomaly in the

234   shear modulus, the crystal structure of Fe$_3$O$_4$ magnetite (Fig. 5a) is compared with those of

235   FeO wüstite (Fig. 5b) and Fe$_2$TiO$_4$ ulvöspinel (Fig. 5c). For cubic wüstite, the anomalous positive

236    $\partial G/\partial T$ in terms of $G = \dfrac{2C_{44} + (C_{11} - C_{12})}{4}$ was proposed to be related to the positive $\partial C_{44}/\partial T$

237   resulting from the lowering C_{44} near its Neel temperature ($T_N \approx 195$ K). As clearly seen in Fig.

238   5(a), this unusual behavior in G for wüstite resulted from the lowering C_{44} can persist up to ~550

239   K, the reason for which is proposed to be due to the magnetoelastic interactions/relaxation from

240   exchange coupling between the neighbor Fe^{2+} ions at the octahedral sites, as suggested by

241   Jackson et al [46] and Isaak et al [47]. By contrast, the shear modulus of the inverse-spinel

242   structured Fe^{2+}(Fe^{2+}Ti^{4+})O$_4$ ulvöspinel increased anomalously with temperatures up to ~225 K,

243   which is ~83 K higher than its curie temperature of $T_C \approx 142$ K [44]. As seen from the crystal

244   structure of Fe$_2$TiO$_4$ ulvöspinel in Fig. 5(c), it is absence of Fe^{3+} ions at the octahedral sites. Thus,

245   the origin of the anomalous shear stiffening with temperatures below ~225 K in Fe$_2$TiO$_4$

246   ulvöspinel was proposed to be related to the presence of Jahn-Teller Fe^{2+} ions at the tetrahedral

247   sites yielding large magnetostriction, rather than the hopping of electrons/charges between Fe^{2+}

248   and Fe^{3+} at the octahedral sites which may be observed in Fe$_2$TiO$_4$-Fe$_3$O$_4$ solid solutions by

249   Ishikawa and Syono [44].

250   For magnetite, the tetrahedral four-coordinated A site is occupied by Fe^{3+} ions, and the

251   octahedral B site is occupied by both Fe^{2+} and Fe^{3+} cations at ambient conditions. According to

252   the previous x-ray diffraction structural studies on single-crystal magnetite, Fe^{3+}-Fe^{2+}-Fe^{3+} ions at

253   the octahedral site may form linear three-Fe-site units (called trimerons) with the three-site

254   distortions, which become charge order below the Verwey temperature of $T_V \approx 122$ K [4, 25].

255   Above the Verwey transition, it is suggested that the inverse-spinel structured magnetite adopts

256   with Fe^{3+} ions in A sites and B sites in a mixed valence $Fe^{2.5+}$ state [15-20]. With increasing

257   temperatures up to ~450 K, we think that the Fe^{3+}-Fe^{2+}-Fe^{3+} ions or formed trimerons may

258   become easy to accommodate atomic displacements/distortions and activate the hopping of

259   electrons or short-range charge ordering between Fe^{2+} and Fe^{3+} at the octahedral sites, resulting

260   in a less symmetrical yet ''ideal'' inverse spinel structure with a small distortion. This short-range

261   correlations in magnetite above the Verwey temperature is further supported by several previous

262   studies on the existence of short-range order of polaronic character in magnetite [15-20], which

263   could be related to a pronounced shear mode stiffening in C_{44} elastic constant [15,16], softening

264   of the surface phonons [17], low-energy fluctuations of the lattice distortions [18], anomalous

265   phonon broadening [19] and nesting features of the Fermi surface [20].

266   On the other hand, because absence of Fe^{2+} ions at the tetrahedral sites of magnetite, the

267   mechanism for the abnormal shear stiffening below ~450 K in magnetite could not be due to the

268   Jahn-Teller effects like Fe_2TiO_4 ulvöspinel [44], or the magnetoelastic interactions between the

269   nearest and next-nearest Fe^{2+} ions as proposed in FeO wüstite [46,47]. Moreover, on the basis of

270   the inverse-to-normal spinel model [21,25], the inverse-to-normal phase transition in magnetite

271   is associated with significant changes in the unit-cell volume and local site symmetry, as well as

272   electrical transport properties. Thus, we rule out the possibility of the inverse-to-normal spinel

273   transition as the mechanism for the anomalous shear stiffening with temperatures of 300~450 K

274   in magnetite. The unit-cell volume, strain, and average Fe-O bond lengths at the octahedral sites

275   for magnetite against temperatures at constant pressure are shown in Figs. S2(b)-(d), indicating

276   that the local atomic distortions in FeO_6 octahedra may be another reason for the

277   temperature-driven anomaly, which is supported by the previous neutron scattering

278 measurements on magnetite where the low-energy fluctuations of the lattice distortions were

279 observed [18]. Therefore, in addition to the short-range charge ordering of Fe^{2+} and Fe^{3+} ions at

280 the octahedral sites of magnetite, the local atomic distortions should also be responsible for the

281 thermal-induced anomaly in the shear modulus above the Verwey temperature. The coupling

282 between local charge ordering and lattice distortions leads ultimately to the structural phase

283 transition with more complicated charge distributions.

284   It is worth noting that the new discovery of the temperature-driven anomaly in the shear

285 properties for Fe_3O_4 magnetite could be also observed in magnetite-based solid solutions or

286 spinel-structured   materials   with   the   composition   of $M_{3-x}N_xO_4$ =

287 $[M^{3+}_{1-x}N^{2+}_x]_{tet}[M^{3+}_{1+x}M^{2+}_{1-x}]_{oct}O_4$ (M = Fe, Co, Ni; N = Zn^{2+}, Mg^{2+}...). Similar to magnetite, the

288 mechanism   for   the   predicted   temperature-induced   anomalies   in

289 $[M^{3+}_{1-x}N^{2+}_x]_{tet}[M^{3+}_{1+x}M^{2+}_{1-x}]_{oct}O_4$ spinels above Verwey transition temperatures would be

290 mainly related to the short-range charge ordering of six-coordinated M^{2+} and M^{3+} at the

291 octahedral sites.

292

293   **IV. CONCLUSIONS**

294   In summary, acoustic velocities and elasticity of Fe_3O_4 magnetite were measured, for the

295 first time, at simultaneously high pressure and high temperature using ultrasonic interferometry

296 in conjunction with synchrotron x-ray diffraction/radiographic imaging techniques. In addition to

297 the pressure-induced softening, we discovered a novel thermal-driven anomaly in the shear

298 modulus of magnetite. Using finite strain approaches, the elastic bulk and shear moduli as well

299 as their pressure and temperature dependences are derived from the directly measured velocities

300 and densities, yielding B_{S0} =173.2(5) GPa, G_0 = 55.5(2) GPa, $\partial B_S/\partial P$ = 2.99(9), $\partial G/\partial P$ = -0.23(3),

301 $\partial B_S/\partial T$ = -0.0209(10) GPa/K, $\partial G/\partial T$ = 0.0042(4) GPa/K, $(\partial^2 B_S/\partial T^2)_P$ = -1.7(1)×1 0^{-5} GPa^2/K^2 and

302 $(\partial^2 G/\partial T^2)_P$ = -2.5(1)×10^{-5} GPa^2/K^2. The anomalous behavior is characterized by the positive

303 temperature dependence and negative pressure derivative for the shear modulus. On the basis of

304 the previous studies [36, 44, 46, 47], we propose that the thermal-induced anomaly in the shear

305 modulus for Fe_3O_4 magnetite is a manifestation of the local atomic distortions and the

306 short-range charge ordering of six-coordinated Fe^{2+}-Fe^{3+} ions at the octahedral sites in the

307 inverse-spinel structure. These results provide us new high-P thermoelasticity data of magnetite,

308 and open a window for good understanding of the underlying mechanism for temperature-driven

309 anomaly in magnetite-based solid solutions and spinel-structured materials for their uses in

310 extreme environments.

311

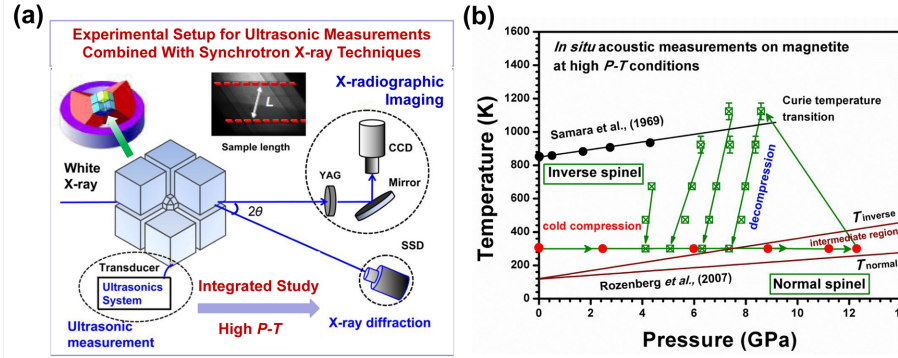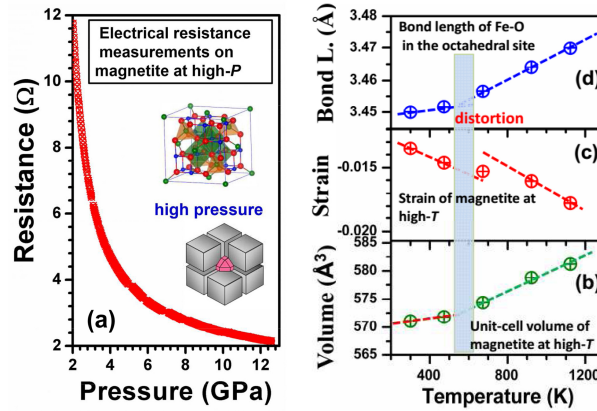## APPENDIX A: EXPERIMENTAL SETUP AND EXPERIMENTAL *P-T* CONDITIONS

FIG. S1. (a). The experimental setup for the present ultrasonic measurements combined with synchrotron x-ray diffraction. (b). Experimental *P-T* conditions for the combination of *in situ* x-ray diffraction and ultrasonic measurements on polycrystalline Fe_3O_4 magnetite, as well as the phase diagram of Fe_3O_4 at high pressure and high temperature based on the previous studies [13, 14]. The red circle symbols represent the *P-T* data points upon cold compression, whereas the crossed-green square symbols are those at high *P-T* conditions during cooling. The black solid line and circles are the phase boundary for paramagnetic-to-ferrimagnetic transition (Curie temperature) determined by Samara *et al*. [13]. The coordination crossover transition boundaries for the inverse-normal conversion are shown in red lines proposed by Rozenberg *et al*. [14], and the in-between area of these two lines represents the intermediate region of the inverse-normal transition.

APPENDIX B: ELECTRICAL RESISTENCE MEASUREMENTS, UNIT-CELL VOLUME, STRAIN AND BOND LENGTH OF MAGNETITE AT HIGH PRESSURE
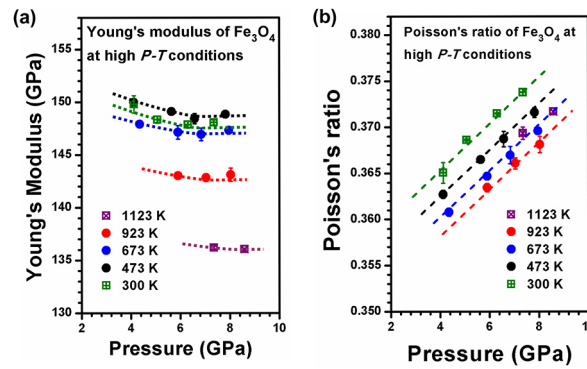
344

345

FIG. S2. (a). Electrical resistance measurements of polycrystalline Fe_3O_4 magnetite at high pressure in a multi-anvil apparatus, showing a continuous decrease in electrical resistance with increasing pressures. (b). Unit-cell volume, (c) strain expressed as $\varepsilon = \left[1 - (V_{(0,T)})/V)^{2/3}\right]/2$, and (d) average Fe-O bond length at the octahedral sites for magnetite against temperatures at constant pressure.

350

APPENDIX C: YOUNG'S MODULUS AND POISSON'S RATIO OF MAGNETITE AT HIGH PRESSURE AND HIGH TEMPERATURE

353

FIG. S3. (a) Young's modulus (E) and (b) Poisson's ratio (v) of Fe_3O_4 magnetite against pressure and temperature, which is derived by applying $E = 9BG/(3B + G)$ and $v = (3B - 2G)/(6B + 2G)$, respectively. The Young's modulus (E) is a measure of the stiffness of a solid material, and Poisson's ratio (v) provides the fundamental metric by which to compare the performance of materials when strained elastically, in

358 comparing a material's resistance to distort under mechanical load rather than to alter in volume. Color

359 lines are eye-guide for isotherms.

360

361 **APPENDIX D: PHYSICAL PROPERTIES OF MAGNETITE AT HIGH PRESSURE AND**

362 **HIGH TEMPERATURE**

363 TABLE SI. Physical properties of Fe_3O_4 magnetite derived from the current ultrasonic
364 measurements in conjunction with synchrotron x-ray diffraction at simultaneously high pressures
365 and temperatures

*P (GPa)	T (K)	ρ (g/cm³)	L (mm)	V_P (km/s)	V_S (km/s)	B_S (GPa)	G (GPa)	v	E (GPa)
8.59	1123	5.293(1)	0.662	6.773	3.061	176.7	49.6	0.372	136.0
7.35	1123	5.254(2)	0.662	6.759	3.077	173.7	49.7	0.369	136.2
8.04	923	5.315(1)	0.661	6.867	3.137	180.9	52.3	0.368	143.1
7.04	923	5.284(1)	0.662	6.843	3.145	177.7	52.3	0.366	142.8
5.90	923	5.249(1)	0.665	6.824	3.161	174.6	52.4	0.363	143.0
7.96	673	5.355(1)	0.660	6.970	3.169	188.5	53.8	0.370	147.3
6.84	673	5.323(1)	0.660	6.948	3.177	185.4	53.7	0.368	146.9
5.90	673	5.295(1)	0.662	6.914	3.191	181.3	53.9	0.365	147.1
4.35	673	5.248(1)	0.665	6.902	3.217	177.6	54.3	0.361	147.9
7.82	473	5.379(1)	0.659	7.015	3.176	192.4	54.3	0.371	148.8
6.57	473	5.344(1)	0.660	7.000	3.184	189.6	54.2	0.370	148.4
5.64	473	5.317(2)	0.662	6.980	3.203	186.3	54.6	0.367	149.1
4.12	473	5.273(2)	0.665	6.968	3.230	182.6	55.0	0.363	150.0
7.35	300	5.386(2)	0.660	7.045	3.163	195.5	53.9	0.374	148.1
6.31	300	5.357(1)	0.660	7.015	3.172	191.8	53.9	0.371	147.9
5.07	300	5.322(2)	0.662	6.995	3.191	188.2	54.2	0.369	148.3
4.12	300	5.295(1)	0.665	6.982	3.219	185.0	54.9	0.365	149.8

366 *The pressures are calculated using the equation: $P = -3K_{S(0,T)} \cdot \varepsilon(1-2\varepsilon)^{2.5}[1+3(4-K'_{S(0,T)})\varepsilon/2]$.
367 The uncertainties are less than 0.3% in elastic wave velocities and ~1.5% in the derived elastic moduli.
368

369

370

371

[1] P. Piekarz, K. Parlinski, A. M. Oleś, Mechanism of the Verwey transition in magnetite, *Phys. Rev. Lett.*, **97,** 156402 (2006).

[2] J. E. Lorenzo, C. Mazzoli, N. Jaouen, C. Detlefs, D. Mannix, S. Grenier, Y. Joly, C. Marin, Charge and orbital correlations at and above the Verwey phase transition in magnetite, *Phys. Rev. Lett.* **101**, 226401 (2008).

[3] Y. Ding, D. Haskel, S. G. Ovchinnikov, Y.-C. Tseng, Y. S. Orlov, J. C. Lang, H. K. Mao, Novel pressure-induced magnetic transition in magnetite (Fe_3O_4), *Phys. Rev. Lett.* **100**, 045508 (2008).

[4] M. S. Senn, J. P. Wright, J. P. Attfield, Charge order and three-site distortions in the Verwey structure of magnetite, *Nature* **481**, 173-176 (2012).

[5] Z. Švindrych, Z. Janů, A. Kozłowski, J. M. Honig, Low-temperature magnetic anomaly in magnetite, *Phys. Rev. B* **86**, 214406 (2012).

[6] D. Levy, R. Giustetto, A. Hoser, Structure of magnetite (Fe_3O_4) above the Curie temperature: a cation ordering study, *Phys. Chem. Miner.* **39**, 169-176 (2012).

[7] S. Ju, T.-Y. Cai, H.-S. Lu, C.-D. Gong, Pressure-induced crystal structure and spin-state transitions in magnetite (Fe_3O_4), *J. Am. Chem. Soc*, **134,** 13780-13786 (2012).

[8] N. Su, Y. Han, Y. Ma, H. Liu, B. Ma, C. Gao, Pressure-induced magnetoresistivity reversal in magnetite, *Appl. Phys. Lett.* **99**, 211902 (2011).

[9] S. Todo, N. Takeshita, T. Kanehara, T. Mori, N. Môri, Metallization of magnetite (Fe_3O_4) under high pressure, *J. Appl. Phys.* **89**, 7347 (2001).

[10] Z. Zhang, S. Satpathy, Electron states, magnetism, and the Verwey transition in magnetite, *Phys. Rev. B* **44**, 13319 (1991).

[11] P. Seneor, A. Fert, J.-L. Maurice, F. Montaigne, F. Petroff, A. Vaurès, Large magnetoresistance in tunnel junctions with an iron oxide electrode, *Appl. Phys. Lett.* **74**, 4017 (1999).

[12] G. Hu, Y. Suzuki, Negative spin polarization of Fe_3O_4 in magnetite/manganite-based junctions, *Phys. Rev. Lett.* **89**, 276601 (2002).

[13] G. A. Samara, A. A. Giardini, Effect of pressure on the Néel temperature of magnetite, *Phys. Rev.* **186**, 577 (1969).

[14] G. K. Rozenberg, Y. Amiel, W. M. Xu, M. P. Pasternak, R. Jeanloz, M. Hanfland, R. D. Taylor, Structural characterization of temperature- and pressure induced inverse-normal spinel transformation in magnetite, *Phys. Rev. B* **75**, 020102(R) (2007).

[15] T. J. Moran, B. Lüthi, Elastic and magnetoelastic effects in magnetite, *Phys. Rev.* **187**, 710 (1969).

[16] H. Schwenk, S. Bareiter, C. Hinkel, B. Lüthi, Z. Kąkol, A. Kozłowski, J. M. Honig, Charge ordering and elastic Constants in $Fe_{3-x}Zn_xO_4$, *Eur. Phys. J. B* **13**, 491 (2000).

[17] M. M. Seikh, C. Narayana, P. A. Metcalf, J. M. Honig, A. K. Sood, Brillouin scattering studies in Fe_3O_4 across the Verwey transition, *Phys. Rev. B* **71**, 174106 (2005).

[18] (a). S. M. Shapiro, M. Iizumi, G. Shirane, Neutron scattering study of the diffuse critical scattering associated with the Verwey transition in magnetite (Fe_3O_4), *Phys. Rev. B* **14**, 200 (1976); (b). Y. Yamada, N. Wakabayashi, R. M. Nicklow, Neutron diffuse scattering in magnetite due to molecular polarons, *Phys. Rev. B* 21, 4642 (1980).

[19] M. Hoesch, P. Piekarz, A. Bosak, M. Le Tacon, M. Krisch, A. Kozłowski, A. M. Oleś, K. Parlinski, Anharmonicity due to electron-phonon coupling in magnetite, *Phys. Rev. Lett.* **110**, 207204 (2013).

[20] A. Bosak, D. Chernyshov, M. Hoesch, P. Piekarz, M. Le Tacon, M. Krisch, A. Kozłowski, A. M. Oleś, K. Parlinski, Short-range correlations in magnetite above the Verwey temperature, *Phys. Rev. X* **4**, 011040 (2014).

[21] S. V. Ovsyannikov, V. V. Shchennikov, S. Todo, Y. Uwatoko, A new crossover in Fe_3O_4 magnetite under pressure near 6 GPa: modification to 'ideal' inverse cubic spinel? *J Phys. Condens. Matter.* **20**, 172201 (2008).

[22] F. Baudelet, S. Pascarelli, O. Mathon, J. P. Itie, A. Polian, J. C. Chervin, Absence of abrupt pressure-induced magnetic transitions in magnetite, *Phys. Rev. B* **82**, 140412(R) (2010).

421 [23] Y. W. Fei, D. J. Frost, H. K. Mao, C. T. Prewritt, D. Haüsermann, *In situ* structure determination of
422 the high-pressure phase of Fe_3O_4, *Am. Mineral.* **84**, 203-206 (1999).

423 [24] H. Kobayashi, I Isogai, T Kamimura, N Hamada, H. Onodera, S. Todo, N. Môri, Structural
424 properties of magnetite under high pressure studied by Mössbauer spectroscopy, *Phys. Rev. B* **73**,
425 104110 (2006).

426 [25] J. F. Lin, J. Wu, J. Zhu, Z. Mao, A. H. Said, B. M. Leu, J. Cheng, Y. Uwatoko, C. Jin, J. Zhou,
427 Abnormal elastic and vibrational behaviors of magnetite at high pressures, *Sci. Rep.* **4**, 06282 (2014).

428 [26] H. -K. Mao, T. Takahashi, W. A. Bassett, G. L. Kinsland, L. Merrill, Isothermal compression of
429 magnetite to 320 kbar and pressure-induced phase transformation, *J. Geophys. Res.* **79**, 1165-1170
430 (1974).

431 [27] M. P. Pasternak, S. Nasu, K. Wada, S. Endo, High-pressure phase of magnetite, *Phys. Rev. B* **50**,
432 6446-6449 (1994).

433 [28] L. S. Dubrovinsky, N. A. Dubrovinskaia, C. McCammon, G. K. Rozenberg, R. Ahuja, J. M.
434 Osorio-Guillen, V. Dmitriev, H.-P. Weber, T. Le Bihan, B. Johansson, The structure of the metallic
435 high-pressure Fe_3O_4 polymorph: experimental and theoretical study, *J. Phys.: Condens. Matter* **15**,
436 7697-7706 (2003).

437 [29] P. Lazor, O. N. Shebanova, H. Annersten, High-pressure study of stability of magnetite by
438 thermodynamic analysis and synchrotron x-ray diffraction, *J. Geophys. Res.* **109**, B05201 (2004).

439 [30] C. Haavik, S. Stølen, H Fjellvåg, M Hanfland, M. Hanfland, D. Häusermann, Equation of state of
440 magnetite and its high-pressure modification: Thermodynamics of the Fe-O system at high pressure,
441 *Am. Mineral.* **85**, 514-523 (2000).

442 [31] L. Gerward, J. S. Olsen, High-pressure studies of magnetite and magnesioferrite using synchrotron
443 radiation, *Appl. Radiat. Isot.* **46**, 553-554 (1995).

444 [32] O. N. Shebanova, P. Lazor, Vibrational modeling of the thermodynamic properties of magnetite
445 (Fe_3O_4) at high pressure from Raman spectroscopic study, *J. Chem. Phys.* **119**, 6100-6110 (2003).

446 [33] S. Isida, M. Suzuki, S. Todo, N. Mori, K. Siratori, Pressure effect on the elastic constants of

447 magnetite, *Physica B* **219-220**, 638-640 (1996).

448 [34] H. J. Reichmann, S. D. Jackbson, High-pressure elasticity of a natural magnetite crystal, *Am. Mineral.*

449 **89**, 1061-1066 (2004).

450 [35] W. Liu, B. Li, Elasticity of amorphous zirconium tungstate at high pressure, *Appl. Phys. Lett.* **93**,

451 191904 (2008).

452 [36] W. Liu, B. Li, L. Wang, J. Zhang, Y. Zhao, Elasticity of ω-phase zirconium, *Phys. Rev. B* **76**, 144107

453 (2007).

454 [37] Y. Zou, T. Irifune, S. Gréaux, M. Whitaker, T. Shinmei, H. Ohfuji, R. Negishi, Y. Higo, Elasticity

455 and sound velocities of polycrystalline $Mg_3Al_2(SiO_4)_3$ garnet up to 20 GPa and 1700 K, *J. Appl. Phys.*

456 **112**, 14910 (2012).

457 [38] Y. Zou, S. Gréaux, T. Irifune, B. Li, Y. Higo, Unusual pressure effect on the shear modulus in

458 $MgAl_2O_4$ spinel, *J. Phys. Chem. C* **117**, 24518-24526 (2013).

459 [39] T. Irifune, Y. Higo, T. Inoue, Y. Kono, H. Ohfuji, K. Funakoshi, Sound velocities of majorite garnet

460 and the composition of the mantle transition region, *Nature* **451**, 814-817 (2008).

461 [40] R. C. Liebermann, Pressure and temperature dependence of the elastic properties of polycrystalline

462 trevorite ($NiFe_2O_4$), *Phys. Earth Planet. Inter.* **6**, 360-365 (1972).

463 [41] B. Li, Compressional and shear wave velocities of ringwoodite $γ$-Mg_2SiO_4 to 12 GPa, *Am. Mineral.*

464 **88**, 1312-1317 (2003).

465 [42] G. R. Rigby, G. B. H. Lovell, A. T. Green, The reversible thermal expansion and other properties of

466 some magnesian ferrous silicates, *Trans. Br. Ceram. Soc.* **45**, 237-250 (1946).

467 [43] A. Roldan, D. Santos-Carballal, N. H. de Leeuw, A comparative DFT study of the mechanical and

468 electronic properties of greigite Fe_3S_4 and magnetite Fe_3O_4, *J. Chem. Phys.* **138**, 204712 (2013).

469 [44] (a). Y. Ishikawa, Y. Syono, Giant magnetostriction due to Jahn-Teller distortion in Fe_2TiO_4, *Phys.*

470 *Rev. Lett.* **26**, 1335 (1971); (b). Y. Syono, Y. Fukai, Y. Ishikawa, Anomalous elastic properties of

471 Fe_2TiO_4, *J. Phys. Soc. Jpn.* **31**, 471 (1971).

472 [45] S. M. Antao, I. Jackson, B. Li, J. Kung, J. Chen, I. Hassan, R. C. Liebermann, J. B. Parise,

473   High-temperature elasticity of magnesioferrite spinel, *Phys. Chem. Miner.* **34**, 345-350 (2007).

474 [46] I. Jackson, S. K. Khanna, A. Revcolevschi, J. Berthon, Elasticity, shear-mode softening and

475   high-pressure polymorphism of wüstite ($Fe_{1-x}O$), *J. Geophys. Res.* **95**, 21671-21685 (1990).

476 [47] D. Isaak, S. Moser, Elasticity of single-crystal wüstite at ambient and elevated temperature from

477   resonant ultrasound spectroscopy, *J. Phys. Chem. Solids* **74**, 879-885 (2013).

478

479

480

481

482

483

484

485

486

487

488

489

490

491

492

493

494

495

496

497

498

499

502 TABLE I. Summary of the elasticity of magnetite, compared with those for other Fe-, Al-, and

503 Si-bearing spinels

Mater.	B_{S0} (GPa)	G_0 (GPa)	$(\partial Bs/\partial P)_T$	$(\partial G/\partial P)_T$	$(\partial Bs/\partial T)_P$ (GPa/K)	$(\partial G/\partial T)_P$ (GPa/K)	$(\partial^2 Bs/\partial T^2)_P$ (GPa^2/K^2)	$(\partial^2 G/\partial T^2)_P$ (GPa^2/K^2)	Ref.
Fe_3O_4 magnetite	173.2(5)	55.5(2)	2.99(9)	-0.23(3)	-0.0209(10)	0.0042(4)	$-1.7(1)\times10^{-5}$	$-2.5(1)\times10^{-5}$	This study
Fe_3O_4	182(9)	---	2.90(1)	---	---	---	---	---	Ju et al.[a]
Fe_3O_4	183(10)	---	4.0(4)	---	---	---	---	---	Mao et al.[b]
Fe_3O_4	215(25)	---	7.5(40)	---	---	---	---	---	Gerward et al.[c]
Fe_3O_4	187.4	49.5	---	---	---	---	---	---	Roldan et al[d]
natural magnetite	186(3)	60 (3)	5.1(1)	-0.1(1)	---	---	---	---	Reichmann et al.[e]
Fe_2TiO_4	121	22.6	---	---	----	0.086	---	-2.344×10^{-4}	Syono et al.[f]
$NiFe_2O_4$	182.3	71.3	4.41	0.38	-0.019	-0.007	---	---	Liebermann[g]
$MgFe_2O_4$	176.3(7)	80.1(2)	---	---	-0.032(3)	-0.0012(1)	---	---	Antao et al.[h]
$MgAl_2O_4$	196.0(9)	109.0(4)	4.60(9)	0.58(3)	-0.022(3)	-0.014(1)	---	---	Zou et al.[i]
Mg_2SiO_4	185(2)	120(1)	4.5(2)	1.5(1)	---	---	---	---	Li[j]

504 [a]First-principles calculations (Ref. 8);

505 [b,c]Static compression experiments (DAC: isothermal results) (Refs. 26, 31);

506 [d]First-principles calculations (Ref. 43);

507 [e]Gigahertz ultrasonic interferometry (DAC) (Ref. 34);

508 [f]Ulatrasonic pulse echo method (Ref. 44);

509 [g,h,i,j]Ultrasonic interferometry (multi-anvil apparatus) (Refs. 40, 45, 38, 41);

510

511

512

513

514

515

516

517

518

519

520

521

522

523

524

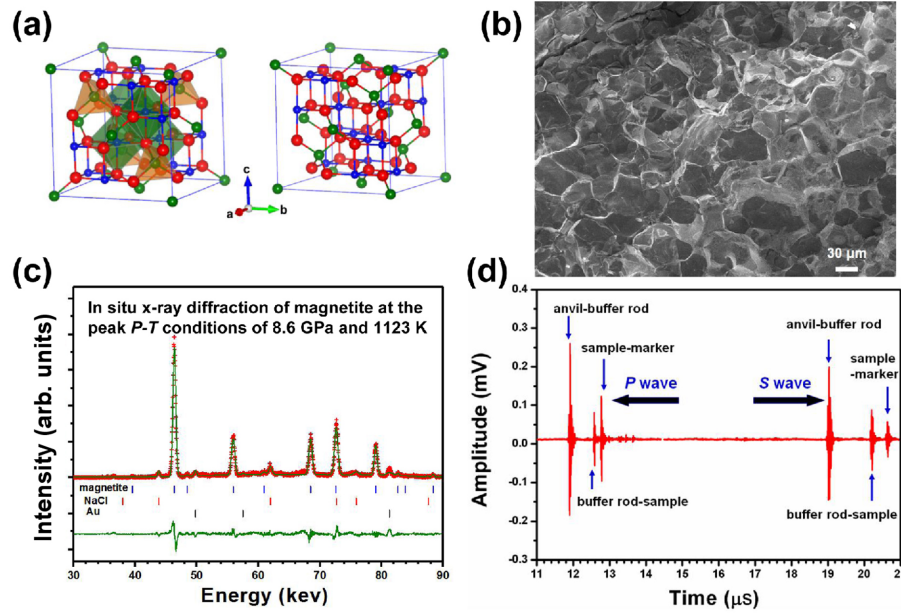525

Figures and Figure captions

529

530

FIG. 1. (a). Crystal structure of Fe_3O_4 magnetite at ambient conditions with a cubic inverse-spinel structure (space group: $Fd\overline{3}m$, No. 227). Large Fe^{3+} ions at tetrahedral sites are represented by green spheres. Red and small blue spheres are oxygen ions and Fe cations (including Fe^{2+} and Fe^{3+}) at the octahedral sites, respectively. (b). SEM image showing the microstructure of the recovered polycrystalline Fe_3O_4 magnetite after the current acoustic velocity measurements. The specimen was free of visible microcracks with an average grain size of about 20~30 μm, exhibiting an equilibrated and homogeneous microstructure. (c). Typical x-ray diffraction pattern of magnetite at the highest *P-T* conditions of 8.6 GPa and 1123 K, suggesting that the specimen is still a cubic spinel structure without the occurrence of other phases such as wüstite and hematite. The solid green line and red cross represent the Rietveld refinement results (PDF: 76-1849) and observed data, respectively, and the solid green curve at the bottom presents the residuals. The vertical bars are the peak positions of the phases present. The peaks of Au and NaCl are from the gold foil and pressure marker used in this study. (d). Waveform data

543   for *P*- and *S*- wave signals of magnetite at the peak *P-T* conditions of 8.6 GPa and 1123 K.
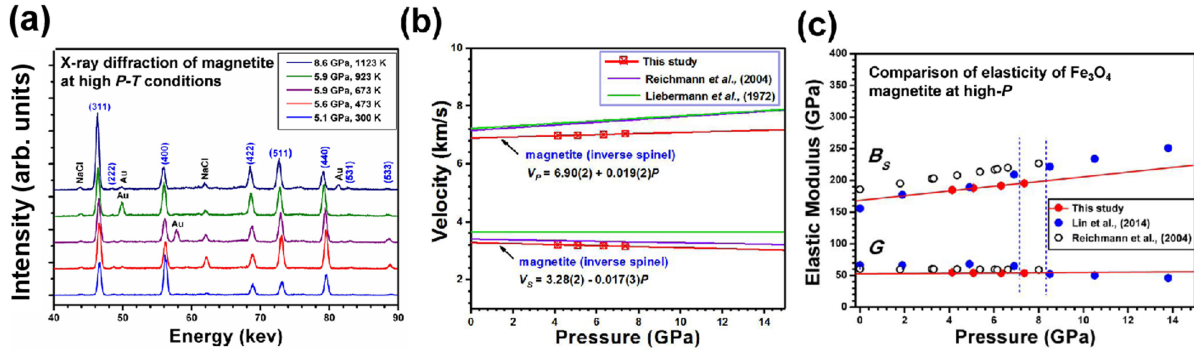
544

546   FIG. 2. (a). Selected x-ray diffraction patterns for Fe_3O_4 magnetite at high pressure and high temperature.

547   The peaks of magnetite are indexed (PDF: #76-1849); and the peaks labeled by Au and NaCl are from the

548   gold foil and pressure marker used in this study. (b). Compressional (V_P) and shear (V_S) wave velocities

549   for Fe_3O_4 magnetite spinel at high pressure and room temperature (after annealing), in comparison with

550   those from the previous studies. The third-order finite strain fits are shown as red-solid lines. (c).

551   Elasticity of bulk and shear moduli of polycrystalline Fe_3O_4 magnetite at high pressure and room

552   temperature, as compared with those from the previous studies by Lin *et al* [25] (blue symbols) and

553   Reichmann *et al* [34] (open-black symbols), respectively. Red lines are the finite strain fits for this study.

554   Blue vertical lines indicate the transition pressure range around ~8 GPa as suggested by Lin *et al* [25].
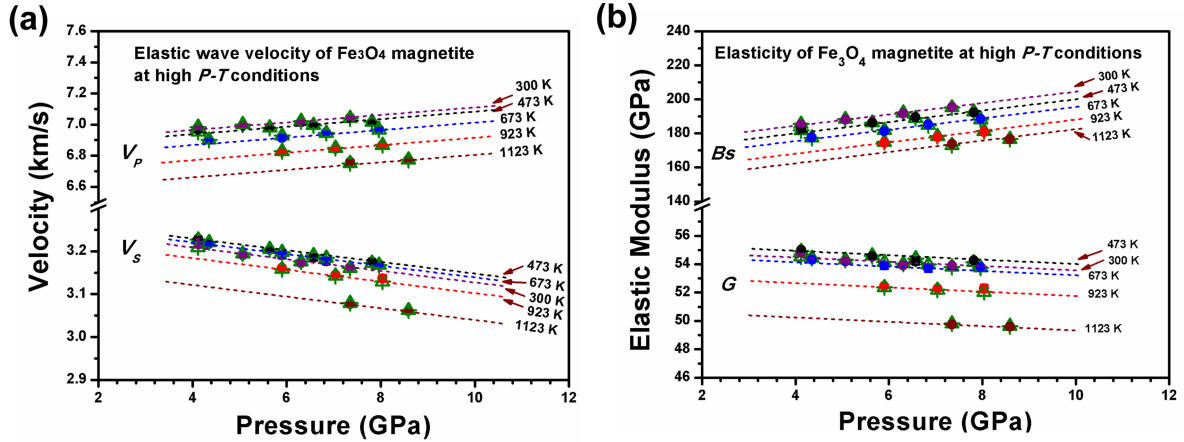
555

556

557

558

559

560

561

562

563

564

FIG. 3. (a). Finite strain fitting (open triangles) and observed (solid circles) results of compressional (V_P)

and shear (V_S) wave velocities of Fe$_3$O$_4$ magnetite as a function of pressure and temperature. (b). Finite

strain fitting (open triangles) and observed (solid circles) results of elastic bulk (B_S) and shear (G) moduli

of Fe$_3$O$_4$ magnetite against pressure and temperature. Error bars indicate two standard deviations. Color

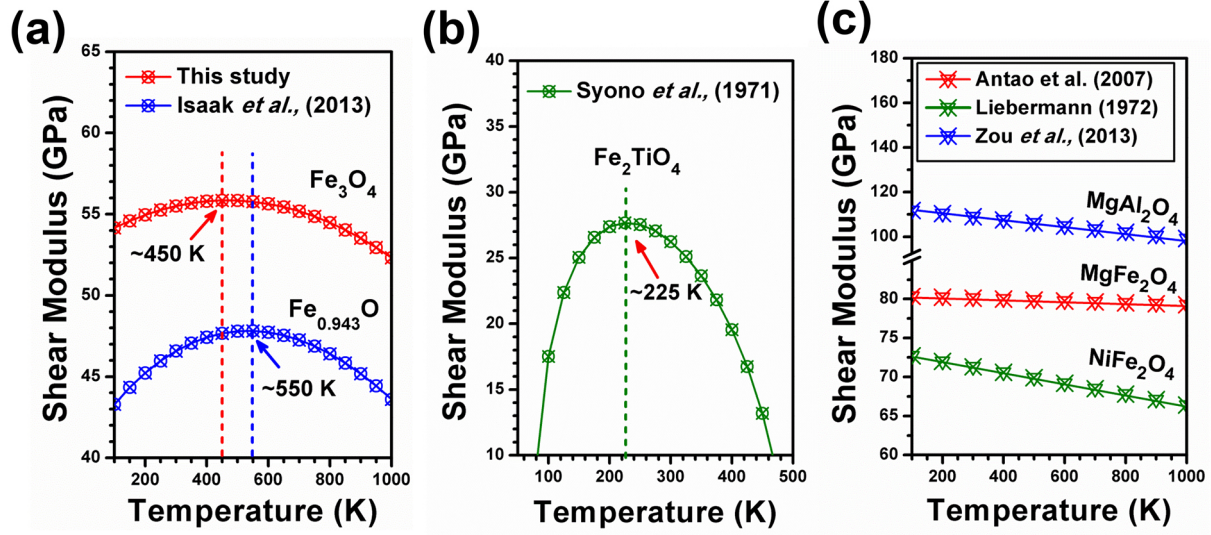lines are eye-guide for isotherms.

582

FIG. 4. (a). Anomalous temperature dependence of shear modulus in spinel-structured Fe_3O_4 magnetite at ambient pressure, in comparison with those for $Fe_{0.943}O$ wüstite, (b) Fe_2TiO_4 ulvöspinel and (c) other spinel-structured materials such as $MgAl_2O_4$, $MgFe_2O_4$ and $NiFe_2O_4$.

586

587

588

589

590

591

592

593

594

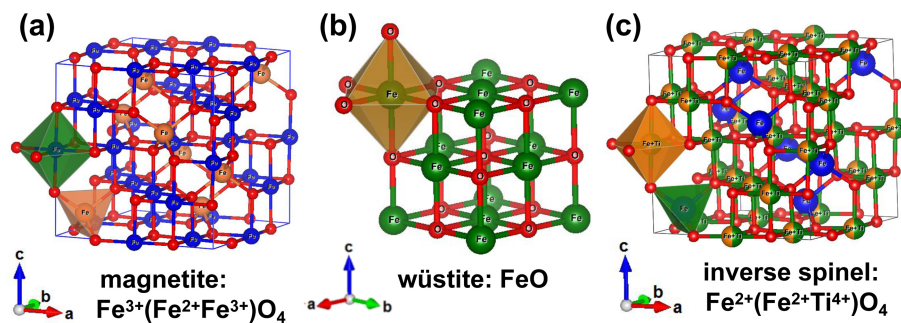595

596

597

598

599

600

FIG. 5. (a). Crystal structure of inverse spinel-structured Fe_3O_4 magnetite at ambient conditions, in comparison with those of FeO wüstite (b) and Fe_2TiO_4 ulvöspinel (c).